Ocean Engineering 304 (2024) 117248

Contents lists available at ScienceDirect

Ocean Engineering

journal homepage: www.elsevier.com/locate/oceaneng

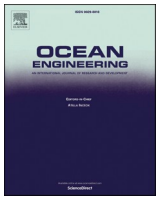

Research paper

Cross-comparison analysis of environmental load components in extreme conditions for pontoon-connected semi-submersible FOWT using CFD and potential-based tools

Ho-Seong Yang [a], Ali Alkhabbaz [b], Watchara Tongphong [a], Young-Ho Lee [a,*]

[a] Center for Offshore Wind & Green Hydrogen Ammonia Research, Korea Maritime and Ocean University, Busan, South Korea
[b] Mechanical Engineering Department, College of Engineering, University of Mosul, Mosul, 41002, Iraq

ARTICLE INFO

Keywords:
Computational fluid dynamics (CFD)
Floating offshore wind turbine (FOWT)
Hydrodynamic coefficient
Middle -fidelity simulation tool
10 MW-Turbine
Pontoon

ABSTRACT

This study focuses on analyzing the load response prediction error of a potential-based tool for a Floating Offshore Wind Turbine (FOWT) with a rectangular pontoon connected to the lower part of the column. The system response was reviewed under extreme environmental loads, and CFD analysis results were compared to analyze the response prediction error contributed by each load component. Based on the CFD free-decay simulation results, we performed potential-based tool calibration by applying damping coefficient and Morison drag coefficient in a composite manner. Through coefficient calibration, the response in the free-decay analysis matched well with the CFD, but there was a significant difference from CFD in the integrated load analysis. Through this study, it was clearly shown that applying an appropriate drag coefficient is very important to implement drag force, especially wave drag force, for FOWT where columns are connected by pontoons. It was confirmed that initial calibration of the potential-based tool using only free-decay analysis is not an appropriate method. However, by applying damping coefficient and Morison drag coefficient in a composite manner when calibrating the potential-based tool based on the free-decay analysis results, it was possible to improve the error by reflecting the current load, and it is expected that the error in the response prediction of the potential-based tool can be further improved through appropriate composite application.

1. Introduction

Recently, with the growing need for marine renewable energy development, active research on Floating Offshore Wind Turbines (FOWT) is underway. Notably, FOWTs offer a significant advantage of being installable and operable even in deep-sea areas. This overcomes the installation constraints related to depth faced by conventional fixed wind power systems, thereby, paving new possibilities for offshore facility development. Among these, FOWTs with semi-submersible structures have gained recognition for their stability and efficiency, attributed to their unique structural features. However, designing and operating these structures require an in-depth understanding of the intricate wind forces and the various factors of the marine environment. Presently, the optimization design work for floating wind systems is carried out using medium-fidelity analysis tools like OpenFAST developed by the National Renewable Energy Laboratory (NREL) (Jonkman, 2013). Yet, these tools require prior knowledge of the platform's hydrodynamic characteristics. Having a potential theory-based hydrodynamic data, assuming the fluid is inviscid and incompressible; adjustments to the model coefficients are needed. Traditionally, these model coefficient values for calibration can be obtained through wave-basin experiments. While experimental model coefficient calibration has its merits in terms of reliability, it is unsuitable for rapid design changes required during optimization. Therefore, alternative methods such as Computational Fluid Dynamics (CFD) simulation tools are more time and cost-effective, and a lot of FOWT coefficient calibration work is being carried out via CFD. Most of this calibration is done to implement the viscous drag effect, and numerous studies have been carried out for simple shapes, such as the DeepCwind semi-submersible structure composed of cylinders, where coefficients were calibrated using CFD, and the calibrated model was cross-validated with CFD results.

Yao et al. (2020) conducted a CFD-based analysis to study the hydrodynamic response of a 6 MW spar-type structure. For this analysis, a

* Corresponding author.
E-mail address: lyh@kmou.ac.kr (Y.-H. Lee).

https://doi.org/10.1016/j.oceaneng.2024.117248
Received 27 October 2023; Received in revised form 29 January 2024; Accepted 20 February 2024
Available online 15 April 2024

reduced-scale model experiment was carried out, and the results were scaled up to full-scale for comparison and validation with CFD and FAST, a potential theory-based analysis tool. Through CFD and moored decay tests, linear and quadratic damping coefficients were derived and applied to the FAST analysis. The experiments were conducted under wave conditions without currents, and the FAST analysis did not use the drag coefficient value. As a result, under regular wave conditions, the heave responses correlated well, but CFD and FAST showed some excessive responses for pitch and surge motions. For pitch motion, the results from CFD and FAST were almost identical. However, for surge motion, the FAST results showed a more exaggerated response than CFD.

The hydrodynamic loads on a floating platform in both transverse and inline directions can be directly determined through the use of the Computational Fluid Dynamics (CFD) approach. Additionally, the analysis incorporates the impact of flow separation induced by viscous flow. Moreover, CFD simulation can explore the intricate flow interaction between the turbine rotor and its wake on one side and between the rotor and the floating platform on the other side (Alkhabbaz et al., 2021, 2022; Yang et al., 2022; Edirisinghe et al., 2023). For this end, it is crucial to perform a methodical comparison between the CFD results for full-scale Floating Offshore Wind Turbines (FOWT) and the corresponding data acquired from diverse numerical tools (Ghalandari et al., 2023; Yang et al., 2023). Yang et al. (2022) utilized OrcaFlex for investigating how varying the number of columns impacts the stability and hydrodynamic behavior of a semi-submersible Floating Offshore Wind Turbine (FOWT).

Benitz et al. (2014) undertook a preliminary code comparison between the high-fidelity analysis tool, CFD, and the engineering tools used for analyzing loads on offshore wind turbines. Their research focused on analyzing hydrodynamic loads, and for this purpose, they kept the DeepCwind Semi-submersible platform stationary. The engineering tool used was HydroDyn from FAST, based on potential theory, and the CFD program was OpenFOAM. The analysis was designed and conducted separately for loads due to currents and waves. Since potential theory is not suitable for calculating loads induced by currents, the Morison equation was used. To calculate loads using the Morison equation, the drag coefficient of the structure was determined based on research analyzing the drag coefficient of a cylinder according to Reynolds (Sarpkaya and Isaacson, 1981; Delany and Sorensen, 1953; Lindsey, 1923; Hussein and Dawood, 2021; Hamdoon, 2020). By applying the appropriate drag coefficient for the analysis, the research found that the wave-induced loads predicted by HydroDyn correlated well with CFD, but the loads induced by currents were somewhat overestimated.

Following their initial studies, Benitz et al. (2015) utilized CFD to intensively analyze the loads exerted by currents on the OC4-DeepCWind semi-submersible structure. They then incorporated these results into the potential flow-based analysis tool, HydroDyn, to enhance the accuracy of their analyses. Tools based on potential theory calculate loads based on wave diffraction, radiation, and other factors. Thus, to account for forces like the drag force from currents, an appropriate drag coefficient needs to be set. Initially, they used a default drag coefficient value of 1 in HydroDyn. This resulted in significantly higher load calculations compared to those obtained from CFD. Afterwards, based on CFD-confirmed loads on the OC4-DeepCWind semi--submersible structure's base and upper offset column, as well as loads on its front, left, and right columns, an extracted drag coefficient was applied. By doing this, the over-predicted loads approached those predicted by CFD, thereby refining the results.

Zhou et al. (2019) performed numerical analyses to investigate the dynamic responses of floating offshore wind turbines subjected to concentrated wave loads. In this study, they also used the OC4-DeepCWind semi-submersible structure as a validation target. They performed CFD analyses on the motion response, hydrodynamics, and mooring line loads of FOWTs for various wave slopes under severe environmental conditions. They compared these with the results from a low-order potential theory-based analysis for specific cases. The results clearly demonstrated that as the wave slope increased, both the motion response and hydrodynamic loads became more nonlinear. During periods of concentrated wave loads, the discrepancy between high-fidelity CFD models and potential theory-based models increased. Comparative studies between the results from high-fidelity CFD and those from reduced-order potential flow theory tools showed a clear discrepancy in predicting hydrodynamic loads and viscous effects. The study confirmed that to fully implement viscous effects in FOWT modeling, as observed in previous researches (Liu et al., 2017, 2018; Cheng et al., 2019; Robertson et al., 2014) and this particular study, one must use CFD to directly solve the Navier-Stokes equations.

Semi-submersible structures, such as the DeepCwind floater, typically possess surge and pitch natural frequencies lower than primary wave frequencies to avoid direct wave excitation. However, in real sea conditions, resonance in surge and pitch can occur due to nonlinear low-frequency waves (Bayati et al., 2014; Simos et al., 2008, 2018). In the FOWT OC5 project and related studies, all the engineering models used underestimated extreme and fatigue loads by up to 20%, with a particularly significant underestimation in the low-frequency domain (Robertson et al., 2017; Pegalajar-Jurado and Bredmose, 2019; AZCONA et al., 2019). To delve deeper into this aspect, two experimental campaigns were conducted in the OC6 project (Robertson et al., 2017, 2020). While these studies incorporated fully quadratic transfer functions (QTFs) for wave excitation and added Morison drag in potential theory-based tools to reduce discrepancies with actual experimental results, the predicted low-frequency response levels still did not measure up to the levels seen in experiments. Furthermore, in the tuned model, collisions were observed. Models using a large Morison drag coefficient and an added damping matrix predicted fixed-condition wave excitation and free decay characteristics better than models without additional damping and a small Morison drag coefficient, but lower estimates were seen at the surge natural frequency (Robertson et al., 2020).

Much like the studies mentioned above, when substituting high-precision experimental data with CFD for tuning mid-fidelity analysis tools essential for FOWT load response analysis, it is imperative that the data derived from CFD is trustworthy. To ensure this, Wang et al. (2021a) compared loads derived from fixed-condition wave excitation experiments with those from CFD analyses using the DeepCWind semi-submersible platform. To ensure the universality of CFD, analyses were conducted based on results from a multitude of institutions using various CFD tools. These institutions included the National Renewable Energy Centre (CENER) of Spain, the Technical University of Denmark (DTU), Dalian University of Technology (DUT), IFP Energies nouvelles (IFPEN), the Maritime Research Institute Netherlands (MARIN), the National Renewable Energy Laboratory (NREL), the Norwegian University of Science and Technology (NTNU), Principle Power, Inc. (PPI), the University of Plymouth (UOP), the University of Strathclyde (UOS), and the University of Ulsan (UOU). Their combined findings demonstrated that CFD's difference-frequency excitation prediction aligned with experimental measurements. This indicates that CFD can be used as a reference for tuning and enhancing mid-fidelity engineering tools and provides a means to better understand the underestimations in the low-frequency domain.

Before embarking on their primary research, Wang et al. (2021b) conducted an evaluation of the uncertainties associated with CFD to ascertain its reliability for refining mid-fidelity analysis tools. Mid-fidelity analysis tools often tend to underestimate the response of semi-submersible platforms and the effects of nonlinear low-frequency waves (Robertson et al., 2017, 2020; Böhm et al., 2020). In this study, a more in-depth analysis was carried out based on the fixed OC5 DeepCwind semi-submersible platform's response in irregular wave conditions. They assessed the response in both the low-frequency and wave frequency domains using two peak PSD-corresponding wave frequencies and the difference frequency excitation between them. The results showed that the potential flow-based analysis tool provided

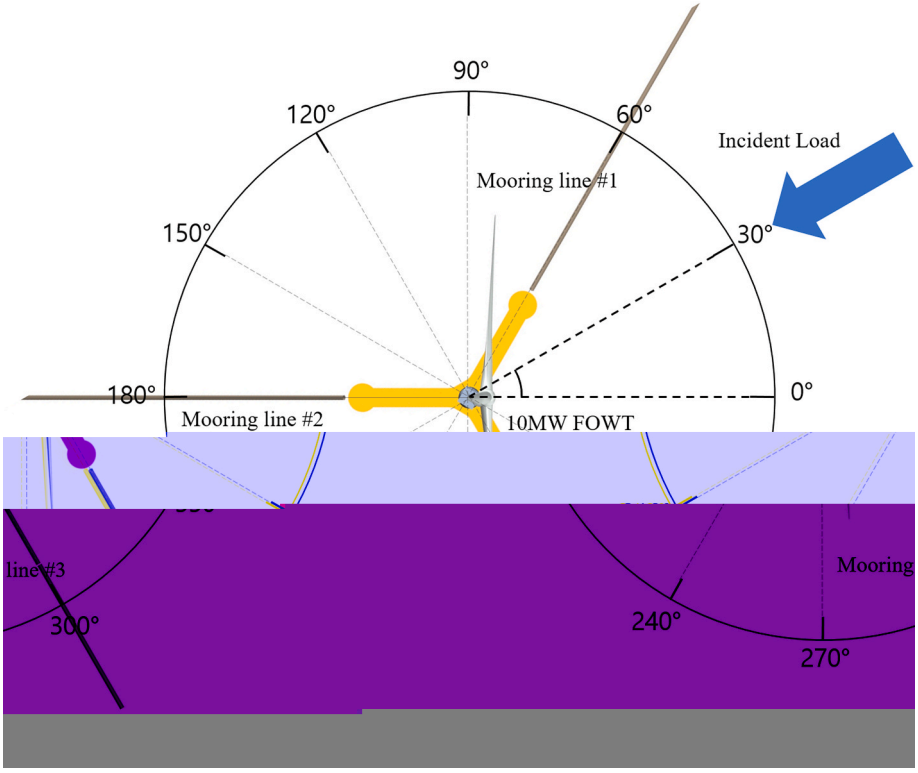

Fig. 1. 10MW FOWT system configuration and incident load direction.

results within an acceptable range when compared to the CFD outcomes that factored in uncertainties for the two wave frequencies. However, the wave load response in the surge direction was much lower than that predicted by the CFD with uncertainties considered.

In the past, free and moored decay and response to wave simulations for floaters have been widely performed. Among them, as mentioned above, many studies have been conducted to compare experimental results with potential flow-based engineering tools and FVM CFD simulation results. These studies show that for simple shapes like cylinders, both types of analysis tools did not show significant errors when compared to the experiments and demonstrated a good agreement in displacement response. However, for more complex structures like the DeepCwind OC4 semi-submersible, a greater discrepancy in surge and pitch responses was observed with potential flow-based tools compared to CFD. But, these discrepancies were improved by applying appropriate drag coefficients (Alkhabbaz et al., 2021; Ghalandari et al., 2023; Yang et al., 2023).

Most of the research on FOWT has been conducted using the DeepCwind semi-submersible platform. While there have been studies on floaters of different shapes, comprehensive research comparing experiments or CFD results of these various shapes with middle-fidelity engineering tool has not been adequately conducted. Generally, to apply viscous drift forces, potential-based tools commonly use drag coefficients for known shapes. In cases like the OC4 model, where the columns of the floater are almost independently configured, this approach tends to be quite accurate. However, for floaters with columns connected by pontoons, the columns are not independent, are performed different hydrodynamic calculations.

Therefore, this study analyzed the error in response prediction using the potential method for an FOWT system with columns connected by pontoons. The analysis was conducted under extreme environmental load conditions, comparing each load components contributing to the error in response with CFD analysis results. The numerical analysis used the potential flow-based middle fidelity engineering tool OrcaFlex, and the CFD tool used for comparison and validation was Star-CCM+.'

Table 1
Design load case for environment load effect evaluation and comparison analysis for different fidelity engineering tools.

Load case no.	Wind speed (m/s)	Wave height (m)	Wave period (s)	Current (m/s)
1	40.28	16.68	13.1	0.77
2	40.28	16.68	13.1	0
3	0	16.68	13.1	0

2. Review of simulation

In this study, based on the 10 MW semi-submersible FOWT system used in a previous study (Yang et al., 2023), we analyzed the load response error arising from environmental factors across engineering tools of varying precision. For the analysis, the FOWT system was designed as depicted in Fig. 1, with the turbine facing the 0-degree direction between line#1 and line#3, and the primary load was applied to the fairlead. This load case was selected based on the integrated load analysis results from the Institute for Advanced Engineering (IAE).

The referenced integrated load analysis was conducted using the middle fidelity analysis tool, OpenFAST. The standards referenced for this analysis were the IEC61400-3-2 international standard (IEC, 2019), the DNV-ST-0119 regulation (DNV, 2021), and the core design load conditions presented in the LIFE50+ project report of the European Union Horizon 2020 (LIFES50+ project, 2015). The same model as the FOWT system in this study was used for this analysis. The hydrodynamic data used in OpenFAST was generated through WAMIT, and the linear damping coefficient, which reflects the damping effect, was extracted from the results of the CFD free decay test.

In Fig. 1, based on the condition where the largest load occurs on the FOWT fairlead in the parking state, represented by the blue arrow, the load case was constructed. While the original OpenFAST integrated load analysis used the JONSWAP model as the wave spectrum, this study applied the Regular wave model for comparative analysis. Moreover,

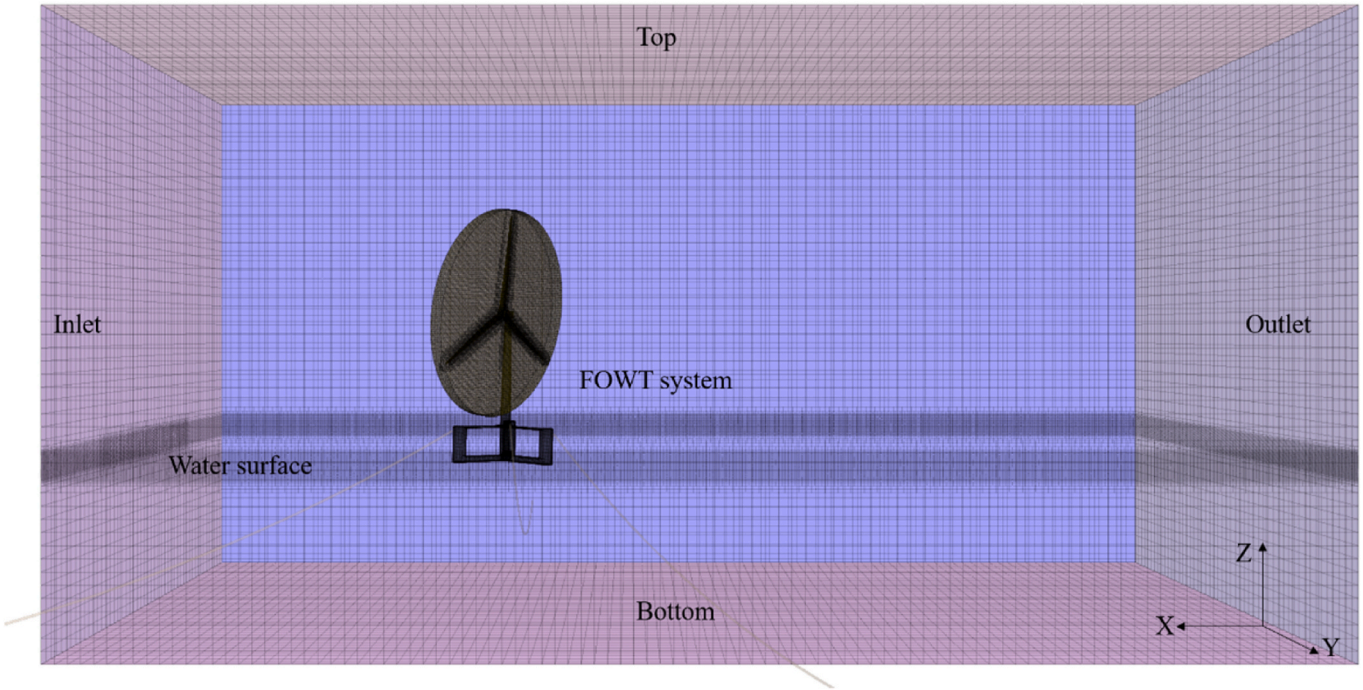

Fig. 2. The Computational Fluid Dynamic simulation domain.

reflecting the point that the error between CFD and the Potential theory-based analysis tool increases as the wave slope increases (Zhou et al., 2019), we aimed to analyze a more pronounced discrepancy by doubling the wave height from the referenced environmental conditions. Consequently, this study used conditions with a wind speed of 40.28 m/s, wave height of 16.68 m, period of 13.1s, and a current of 0.77 m/s. And the 1st order regular wave type is adapted as the wave model. As shown in Table 1, to analyze the discrepancies arising from each load factor in detail, based on load case #1, load conditions without considering the current and conditions without considering both the current and wind speed were structured as analysis cases for comparative analysis.

3. Computational model

The CFD and potential flow-based engineering tool used in this study is the same as the model from the previous study (Yang et al., 2023), so the description for this part has been kept brief.

3.1. CFD model

CFD is a methodology used for the numerical analysis of fluid flow, heat transfer, and related phenomena. For incompressible fluids, it is based on the following Navier-Stokes equations.

$$\frac{\partial u}{\partial t} + u \cdot \nabla u = -\frac{1}{\rho}\nabla p + \nu \nabla^2 u \tag{1}$$

Here, u represents the fluid velocity vector, t is time, p denotes pressure, ρ is the density, ν stands for the kinematic viscosity coefficient. Equation (1) is discretized and then numerically solved under given boundary conditions and preset initial conditions. In CFD, turbulence is a complex phenomenon that encompasses motions of various temporal and spatial scales. Due to such complexity, direct computation is generally challenging. To address this, various turbulence models have been developed by either averaging or filtering the Navier-Stokes equations to derive modified equations that account for the effects of turbulence. In this study, the Shear Stress Transport (SST) turbulence model was employed, which combines the advantages of both the k-epsilon and k-omega models. The equations for the SST turbulence model are given by equations (2) and (3).

Turbulent kinetic energy(k) equation:

$$\frac{\partial(\rho k)}{\partial t} + \frac{\partial(\rho k u_j)}{\partial x_j} = \frac{\partial}{\partial x_j}\left[\left(\mu + \frac{\mu_t}{\sigma_k}\right)\frac{\partial k}{\partial x_j}\right] + P_k - \beta^* \rho \omega k \tag{2}$$

Specific dissipation rate(ω) equation:

$$\frac{\partial(\rho \omega)}{\partial t} + \frac{\partial(\rho \omega u_j)}{\partial x_j} = \frac{\partial}{\partial x_j}\left[\left(\mu + \frac{\mu_t}{\sigma_k}\right)\frac{\partial \omega}{\partial x_j}\right] + \alpha \frac{\omega}{k} P_k - \beta \rho \omega^2 \tag{3}$$

Here, P_k represents the production term, μ_t is the turbulent viscosity coefficient, σ_k, σ_ω are the dissipation rates and α, β, β^* are model constants. The SST model uses a special mixed function to transition between the k-epsilon and k-omega models. By so doing, it capitalizes on the strengths of the k-omega model near the wall and the advantages of the k-epsilon model away from the wall

3.2. Simulation set up

In this study, simulations were performed for two scenarios: free decay motion analysis and extreme environmental load response analysis. The free decay motion was conducted to derive the Morison drag coefficient and damping coefficient needed for implementing viscous effects in the potential flow-based analysis tool, and analyses were performed for Surge, Heave, Pitch, and Yaw movements. For computational efficiency, the turbine, nacelle, and tower structures were excluded from the free decay motion analysis, and only the floater was subjected to the simulation. However, the weight and moment of inertia applied to the floater were based on the values when all structures were combined. The grid on the floater surface was structured so that the CFL number was approximately 1, and the grid configuration for the entire domain, including the water surface and surrounding areas, followed the same configuration used in the previous study (Yang et al., 2023). The time step for the free decay motion analysis was set to 0.025s, enhancing precision using the 2nd order time discretization method, and the extreme environmental load response analysis applied a 0.05s time step, employing the 1st order time discretization method for simulation

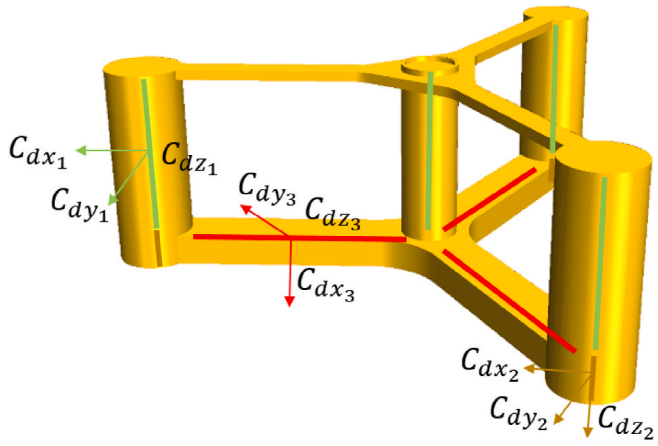

Fig. 3. Morison element drag coefficient.

Table 2
Drag coefficient values of columns and pontoons comprising the platform.

	Top column			Bottom column			Pontoon		
C_d	x_1	y_1	z_1	x_2	y_2	z_2	x_3	y_3	z_3
	0.61	~	0.8	0.61	~	2.4	2.0	3.0	0.2

stability.

This study was conducted under more extreme conditions compared to previous research, especially with the wind speed set higher at 40.28 m/s than what was applied in previous studies. However, since the turbine is in a non-rotating "parking" condition, it was determined that there was no need to modify the grid configuration for the turbine section. As shown in Fig. 2, the grid size for the water surface area remained the same in the x and y directions, considering the increased period. Still, reflecting the increase in amplitude, the area extending to 1.5 times the amplitude in the vertical direction was redefined as the water surface area for grid configuration.

3.3. Potential flow based model

Potential flow theory disregards the viscosity of the fluid and only applies to flows that are irrotational, meaning they have no vorticity. Utilizing this theory, one can define the velocity potential function of the fluid, and from this, the characteristics of the flow can be understood.

Potential Velocity, Φ :

The velocity of the fluid can be expressed as the spatial gradient of the potential function, as shown in equation (4):

$$u = \nabla\Phi \tag{4}$$

Irrotational Condition is given by equation (5):

$$\nabla \times u = 0 \tag{5}$$

Such potential flow models satisfy the following Laplace equation, as shown in equation (6):

$$\nabla^2\Phi = 0 \tag{6}$$

Potential flow theory is especially useful for analyzing low-viscosity flows, flows at infinity, and the initial flows around complex shapes. In this study, it was utilized to calculate the platform's hydrodynamic data, such as the added mass and damping, as well as the Response Amplitude Operators (RAOs).

The viscous effect is challenging to implement using only a Potential flow-based model, so the Morison element and damping coefficient were introduced to account for the viscous terms. Using only one of the drag coefficient (Morison) or damping coefficient for calibration makes it difficult to accurately capture viscous effects such as the damping portion or the drift effects caused by currents and wave viscosity. Hence, both elements were employed in combination. To employ this composite method, the drag coefficient was selected first, followed by the damping coefficient. The drag coefficient was applied with reference to values presented by A. Srinivas et al. (2023) and V. Venugopal et al. (2009), as shown in Fig. 3 and Table 2. For platforms with an applied drag coefficient, the damping coefficient was determined by adjusting it to best match the CFD free decay motion analysis results, as shown in Fig. 4.

4. Result

4.1. Free decay simulation

Fig. 5a compares the predicted results of surge free decay motion over time between the CFD and Potential-based analysis tools. In the first damping section, both methods showed a significant damping magnitude, and this magnitude followed almost identical patterns. However, in the second and third sections, the Potential method exhibited a smaller damping magnitude. While there was a slight difference in the initial damping magnitude, subsequently, the damping magnitudes from both methods appeared almost similar. Fig. 5 is a graph showing the peak values that occurred in each damping section. After the first damping, the Potential method showed a smaller damping magnitude in the second damping section compared to the CFD. Subsequent peaks in both analytical tools showed similar damping motions within a range of 1~4m. Table 3 displays the damping ratio and difference from the surge free decay simulation results of CFD and the

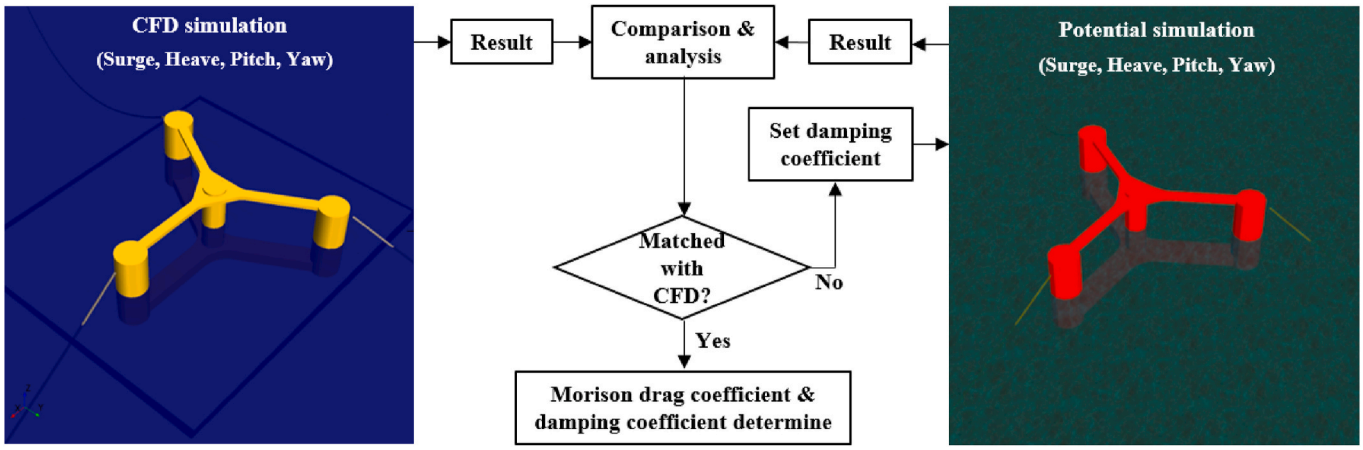

Fig. 4. Potential flow base method damping coefficient determining procedures.

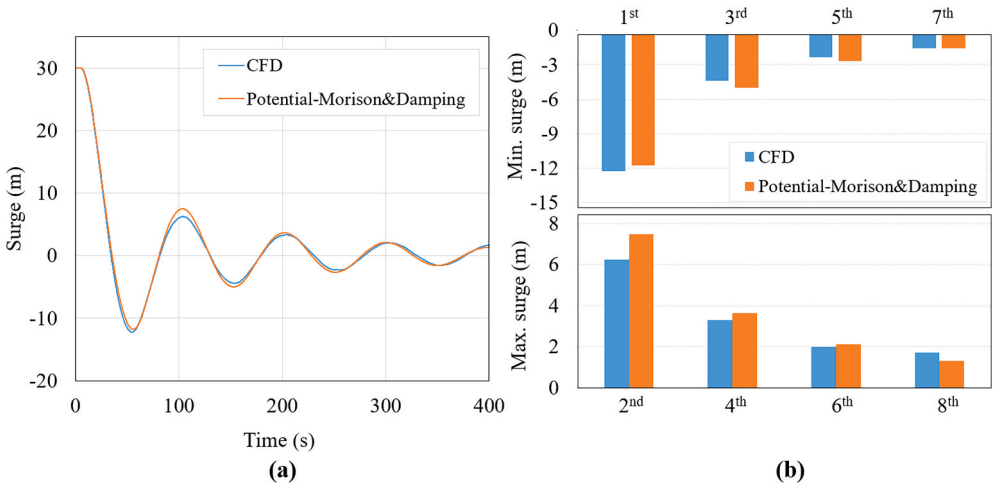

Fig. 5. Surge free decay simulation result. (a) Time series result. (b) Peak value result.

Table 3
Surge free decay simulation damping ratio result comparison.

Damping ratio	CFD	Potential - Morison&Damping	Difference (%)
ζ_1	0.437	0.461	11.480
ζ_2	0.576	0.648	1.554
ζ_3	0.725	0.693	−1.016
ζ_4	0.729	0.731	−1.678
ζ_5	0.768	0.757	−2.242
ζ_6	0.823	0.773	−2.898
ζ_7	0.918	0.784	−3.397
ζ_8	0.893	0.789	−3.720

Table 5
Heave free decay simulation damping ratio result comparison.

Damping ratio	CFD	Potential - Morison&Damping	Difference (%)
ζ_1	0.621	0.478	−9.860
ζ_2	0.597	0.691	−1.634
ζ_3	0.677	0.765	−0.582
ζ_4	0.722	0.812	0.082
ζ_5	0.768	0.843	0.383
ζ_6	0.794	0.864	0.462
ζ_7	0.891	0.881	0.550
ζ_8	0.904	0.893	0.638

Potential method. The largest damping was observed in the first section, with the error being the highest at 11.48%. In subsequent sections, the Potential analysis tool showed a damping motion with an error below 4%. While the error rate increased progressively with the damping progression, this error decreased to a negligible level as the damping magnitude reduced. Table 4 shows the difference in peak values between the two analysis tools in each damping section. A peak value difference of 1m was observed in the second section, but other sections showed a difference within 0.5m, and on average, a very low peak error of 0.562m was confirmed.

Table 4
Surge free decay simulation peak value difference result.

Extreme. value(ABS) Difference (each half period)	CFD vs Morison & Damping correction								
	1st	2nd	3rd	4th	5th	6th	7th	8th	RMS
Surge (m)	−0.478	1.243	0.592	0.338	0.350	0.109	0.030	−0.397	**0.562**

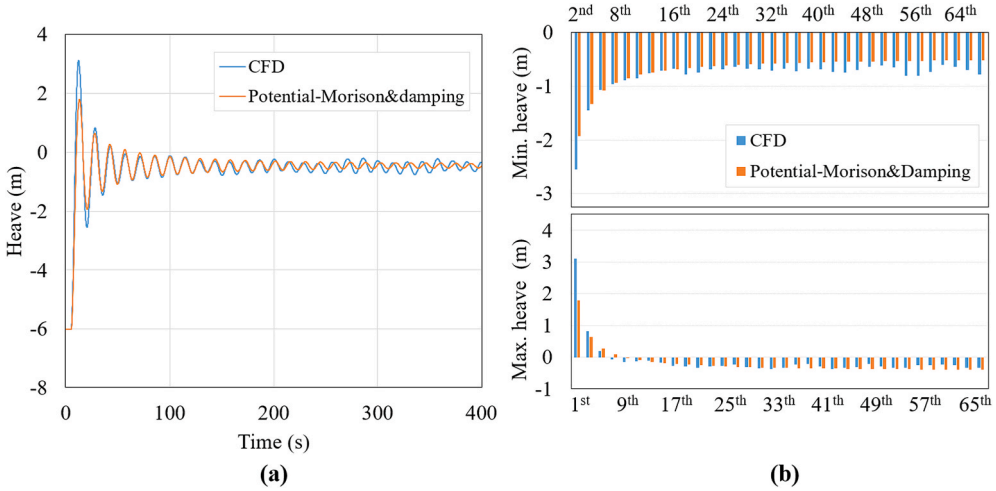

Fig. 6. Heave free decay simulation result. (a) Time series result. (b) Peak value result.

Table 6
Heave free decay simulation peak value difference result.

Extreme. value(ABS) Difference (each half period)	CFD vs Morison & Damping correction								
	1st	2nd	3rd	4th	5th	6th	7th	8th	RMS
Heave (m)	−1.326	−0.617	−0.193	−0.129	0.073	0.004	0.021	−0.025	**0.524**

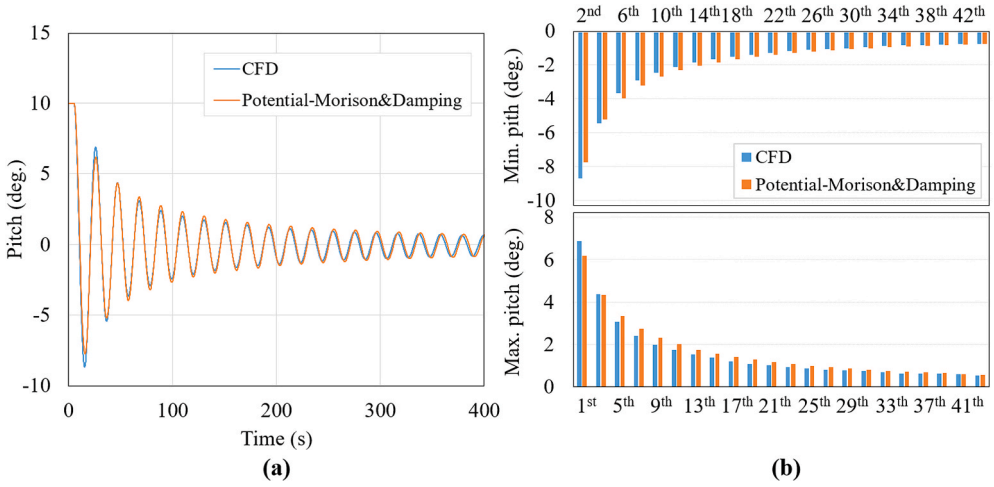

Fig. 7. Pitch free decay simulation result. (a) Time series result. (b) Peak value result.

Fig. 6a depicts a graph comparing the Heave free decay motion over time between the two analysis tools (CFD and Potential), while Fig. 6b shows a graph comparing the peak values occurring in each damping section. Similar to the Surge results, a significant damping occurred in the initial damping section, and the differences in the first and second peak values were analyzed to be approximately 1m and 0.5m, respectively. In the subsequent sections, both methods showed similar damping motions. After 200s, the CFD results consistently showed a reduction in oscillation by about 0.5m, displaying irregular damping. This phenomenon appears to be influenced by the vortex generated during the up-and-down motion in the CFD, which isn't reflected in the potential flow analysis. Hence, the Potential method displayed a stable response. In the absence of waves, this difference could be a major source of discrepancy between the two analyses. However, considering the substantial impact of wave amplitude on the platform when waves are present, this error isn't anticipated to be a significant issue in practice. Table 5 presents the damping ratio from the Heave free decay motion results between the two analysis tools. An error of 9.8% appeared in the first damping section, but subsequent sections showed a low error of less than 1%. In Table 6, looking at the peak error in the second section, the Potential results showed a value about 0.6m lower than the CFD. In a Heave load response with a damping magnitude of 4m, this could act as a significant error. Such discrepancies indicate that there might be differences in load responses with similar oscillation amplitudes between the two analytical approaches.

Fig. 7a and b display the results comparing the time-series data and peak values of the pitch free decay motion. From these results, one can observe a good overall match between the pitch free decay motion outcomes of the two analysis tools. According to Table 7, the most significant damping appeared in the first damping section, but a very low error of less than 1% was observed. This low error is believed to be a result of the high damping ratio. In Table 8, when looking at the peak value discrepancies, the CFD results showed values that were 0.924 deg and 0.771 deg higher than the Potential analysis for the first and second peak values, respectively. Thus, under load conditions with large pitch responses, an error of around 1.5–2deg might be evident. The RMS value of the overall peaks is 0.474 deg, implying an anticipated average pitch response amplitude discrepancy of about 1deg between the two analysis tools.

Fig. 8a and b display the comparison graphs for the results of free decay motion in the yaw direction. While the peak values themselves appeared similar between the two analyses, a distinct period discrepancy emerged, contrasting with previous results. This error is believed to be due to the yaw motion being more influenced by the mooring lines compared to other motions, and it is surmised to have originated from the difference in mooring line load calculation methods between the two analysis tools. According to Tables 9 and 10, a minor discrepancy was evident in the initial damping section, but the subsequent damping portions showed similar damping ratios between the two analyses. The average discrepancy in the peak values for yaw motion was found to be

Table 7
Pitch free decay simulation damping ratio result comparison.

Damping ratio	CFD	Potential - Morison&Damping	Difference (%)
ζ_1	0.833	0.784	1.018
ζ_2	0.792	0.817	0.001
ζ_3	0.796	0.840	−0.005
ζ_4	0.818	0.871	0.993
ζ_5	0.840	0.881	0.570
ζ_6	0.891	0.897	1.280
ζ_7	0.887	0.907	0.846
ζ_8	0.913	0.910	0.823

Table 8
Pitch free decay simulation peak value difference result.

Extreme. value(ABS) Difference (each half period)	CFD vs Morison & Damping correction								
	1st	2nd	3rd	4th	5th	6th	7th	8th	RMS
Pitch (deg)	−0.924	−0.711	−0.236	−0.018	0.317	0.275	0.301	0.338	**0.474**

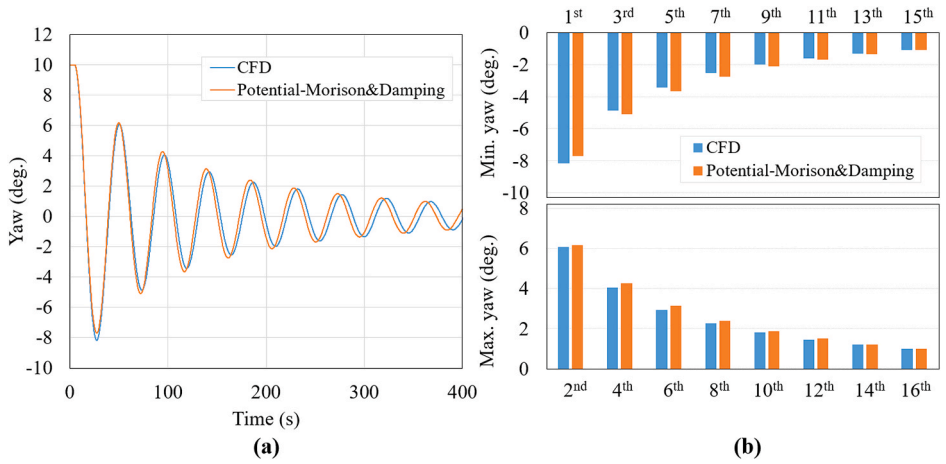

Fig. 8. Yaw free decay simulation result. (a) Time series result. (b) Peak value result.

Table 9
Yaw free decay simulation damping ratio result comparison.

Damping ratio	CFD	Potential - Morison&Damping	Difference (%)
ζ_1	0.784	0.784	3.331
ζ_2	0.768	0.812	1.712
ζ_3	0.815	0.831	0.815
ζ_4	0.838	0.846	0.241
ζ_5	0.852	0.857	−0.142
ζ_6	0.861	0.866	−0.422
ζ_7	0.874	0.874	−0.627
ζ_8	0.885	0.880	−0.793

0.248 deg, which is relatively small.

Fig. 9 is a graph comparing the time intervals of the peaks, specifically the half-period values of free decay motion responses for each motion. This graph predominantly showcases the results from regions where significant damping occurs. In most motions, the Potential analysis exhibited a period that was approximately 0.5∼1s shorter than that

Table 11
Free decay simulation average period difference result.

Average period difference	CFD vs potential morison & damping correction (%)
Surge	−2.2
Heave	0.19
Pitch	0.48
Yaw	−1.91

Table 10
Yaw free decay simulation peak value difference result.

Extreme. value(ABS) Difference (each half period)	CFD vs Potential Morison & Damping correction								
	1st	2nd	3rd	4th	5th	6th	7th	8th	RMS
Yaw (deg)	−0.473	0.098	0.228	0.221	0.227	0.201	0.206	0.150	**0.248**

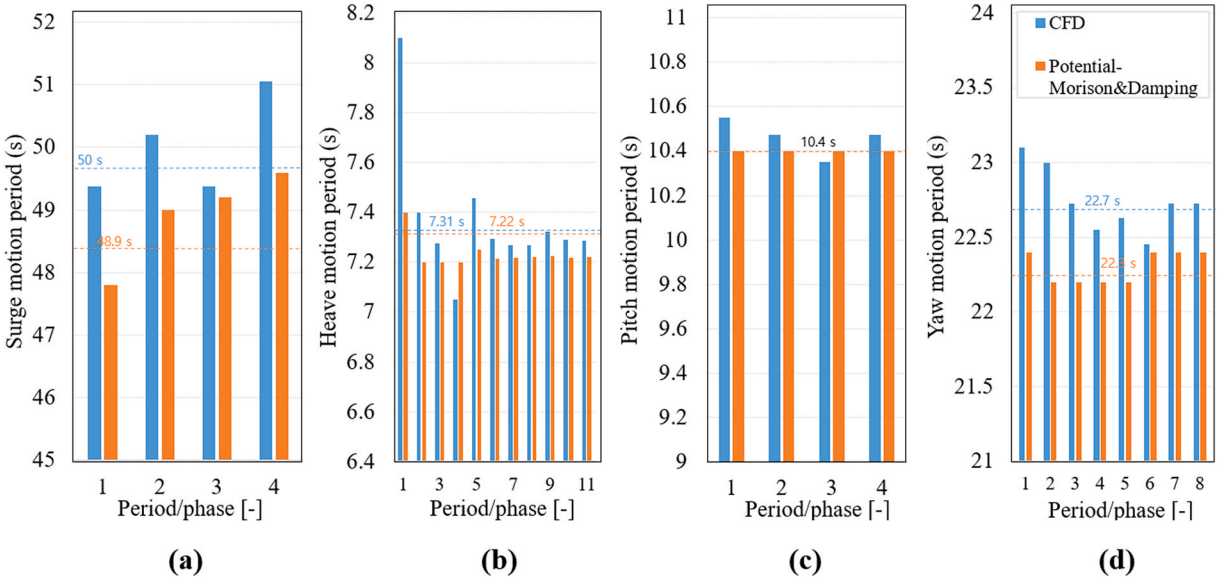

Fig. 9. Free decay simulation result period comparison. (a) Surge motion period. (b) Heave motion period. (c) Pitch motion period. (d) Yaw motion period.

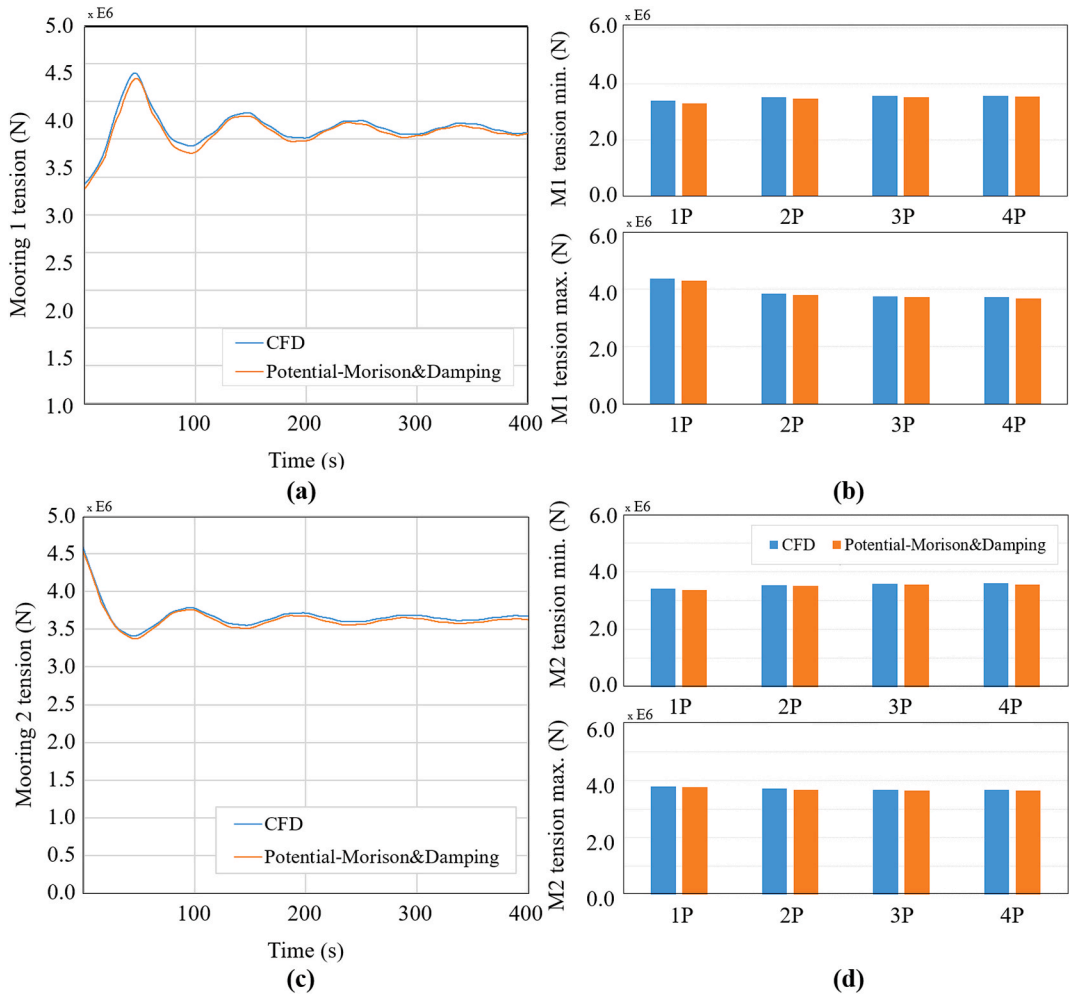

Fig. 10. Surge free decay simulation fairlead tension analysis result. (a) M1 fairlead tension time series. (b) M1 fairlead tension peak value. (c) M2 fairlead tension time series. (d) M2 fairlead tension peak value.

Table 12
M1 maximum tension different codes comparison result.

Max M1 tension difference (each half period) (%)	CFD vs Morison & damping correction				
	1P	2P	3P	4P	RMS
Mooring M1 effective tension	−1.648	−1.223	−0.670	−0.916	**1.172**

of CFD. Table 11 presents the discrepancies between the analysis tools based on the averaged damping motion periods over 400s. In the Surge motion, the largest period discrepancy of 2.2% was observed, yet due to its long periodic nature, the difference wasn't significantly pronounced over 400s. In contrast, the yaw motion, having a shorter period than surge, manifested a noticeable period discrepancy as the free decay motion progressed. For the Heave motion, a very low discrepancy of 0.19% was identified, but due to its shorter period, it exhibited a period discrepancy similar to yaw in the latter part of the free decay motion.

Fig. 10a and c display graphs representing the tension observed at the fairlead of M1 (Mooring line #1) and M2 (Mooring line #2) due to surge free decay motion. M3 (Mooring line #3), being positionally symmetrical to M1, was excluded from the results. Through these graphs, it was evident that the mooring line tension between the two analysis tools showed almost identical patterns with only minor discrepancies. The peak value discrepancy, observable in Fig. 10b,d and Table 12, also demonstrated that the results from the potential flow-based analysis closely matched those from CFD, exhibiting a very low average error of 1.172%.

4.2. Code compatibility check

For the turbine, the reliability of the CFD analysis results for the FOWT turbine used in this study was sufficiently ensured by conducting a CFD mesh sensitivity test using data from the DTU-10MW turbine report (Bak et al., 2013). On the other hand, for the floater, it was a newly designed floating body during the project, and there are still no experimental data on the load response of the floater. Therefore, a mesh sensitivity test was conducted based on the results of finely-configured CFD, and the determined grid configuration was applied in this analysis. Since neither of these two main parts was based on CFD settings derived from contrasting with experimental results, a compatibility test between the two analysis tools was performed before setting CFD as the ground truth and proceeding with analysis.

The compatibility test was conducted using the system under lower steepness waves/mild conditions with a wave height of 6 m and a wave period of 13.1 s, in the absence of currents and wind. A 1st order regular wave was used as the wave model. Fig. 11 shows the results of the compatibility test conducted between the CFD and the Potential method tool. To evaluate the error rate between analysis tools as well as the safety and stability of the system simultaneously, some load response results were normalized using reference values. For the mooring lines, nondimensionalization was based on the breaking load (MBL) of the mooring lines used in this study, which is 21,179 kN. Surge was

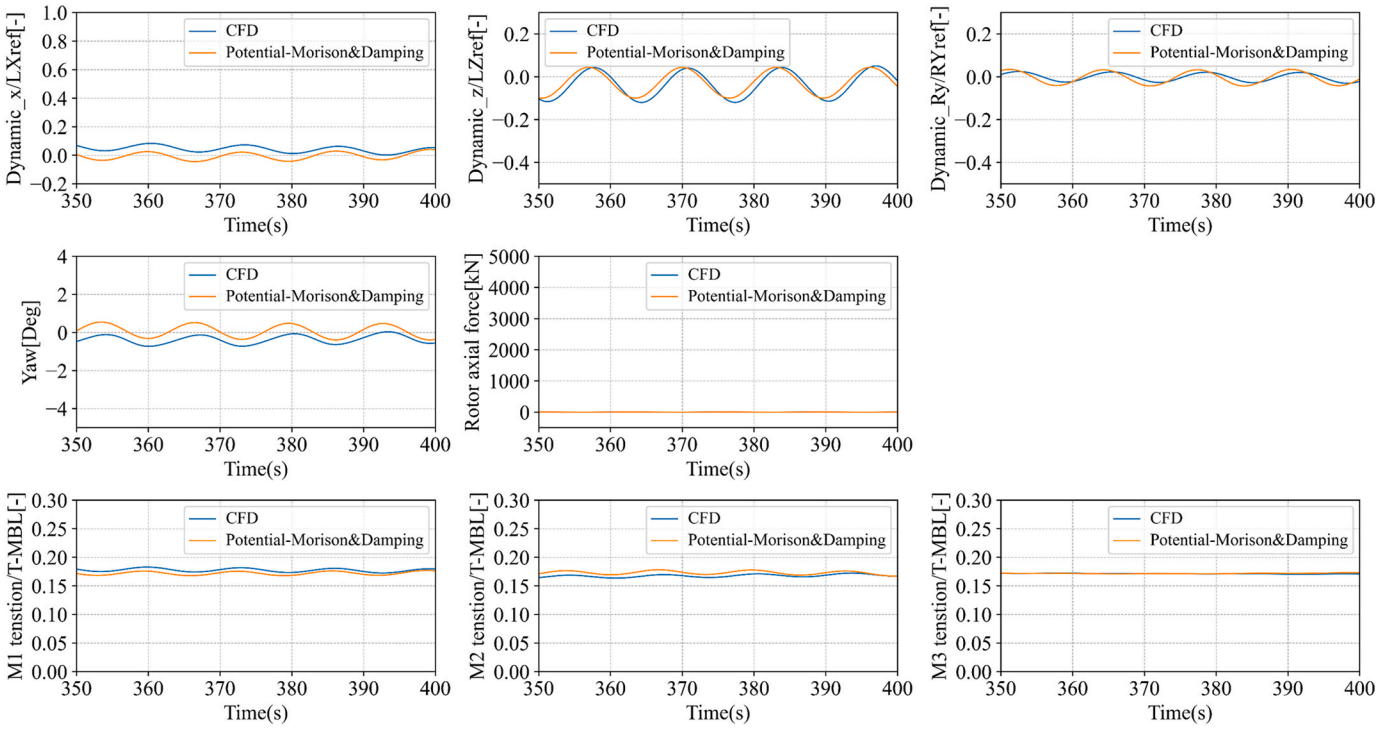

Fig. 11. Compatibility test time series results (Blue line: CFD, Orange line: Potential method tool, wave height: 6m, period: 13.1s).

nondimensionalized based on the point 63 m away in the horizontal direction from the incident load direction where the breaking load occurs. Heave and the point where the air-gap becomes zero, set at 16.5 m, were used as the basis for nondimensionalization, and pitch was nondimensionalized based on the capsizing point at 18.5°. Upon examining the results, it can be seen that important responses for FOWT load response analysis, such as surge, heave, pitch, and yaw are well matched between the two analysis tools. Not only the motion responses but also the tension analysis results of the mooring lines connected to the floater were found to be well aligned. Based on this completed compatibility test with CFD, this study conducted a load response analysis under extreme environmental conditions with both CFD and the potential method tool.

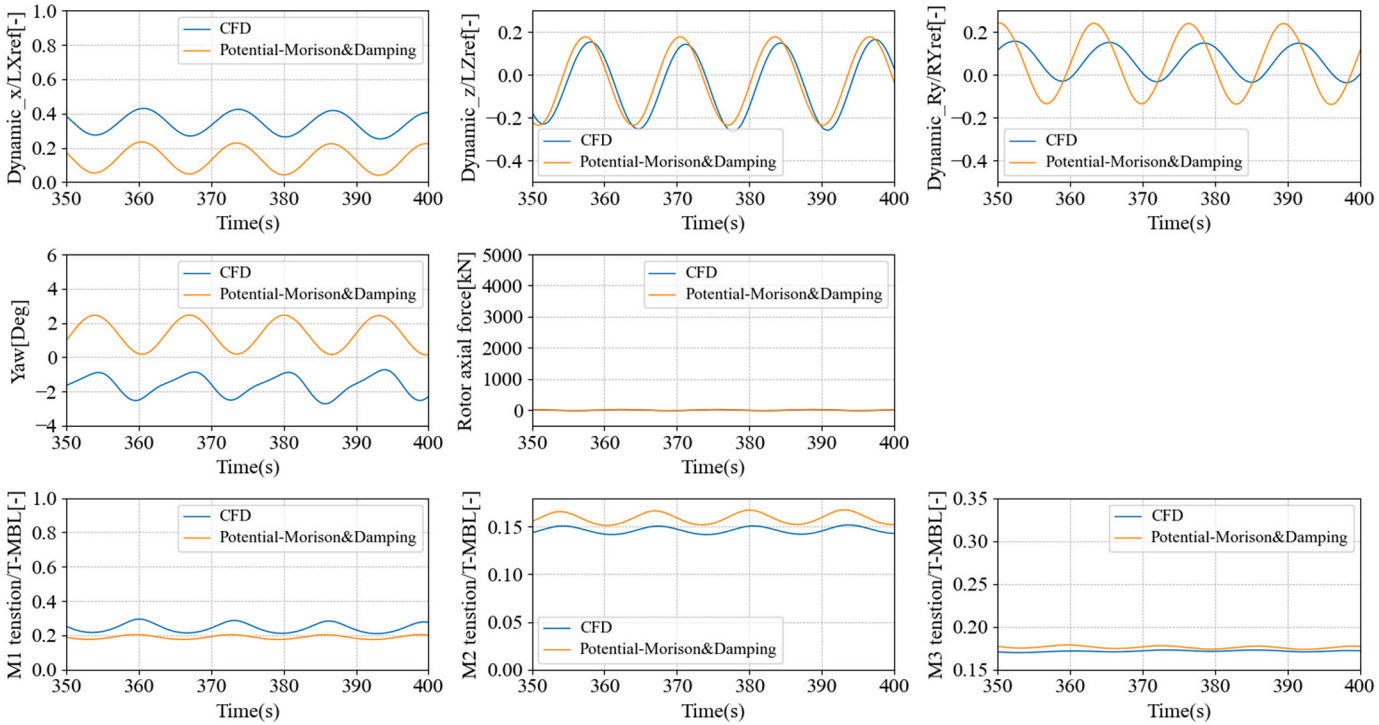

Fig. 12. Wave only considered extreme condition code comparison time series load response result.

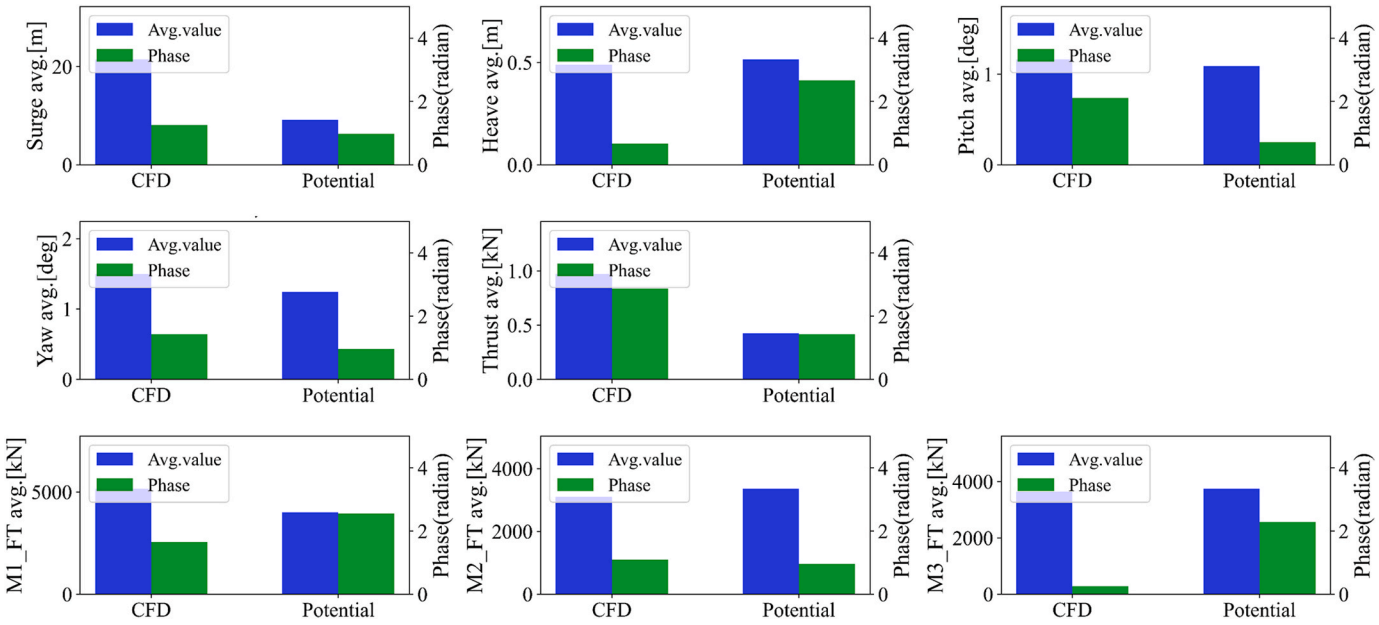

Fig. 13. Wave only considered extreme condition load response average and phase result code comparison.

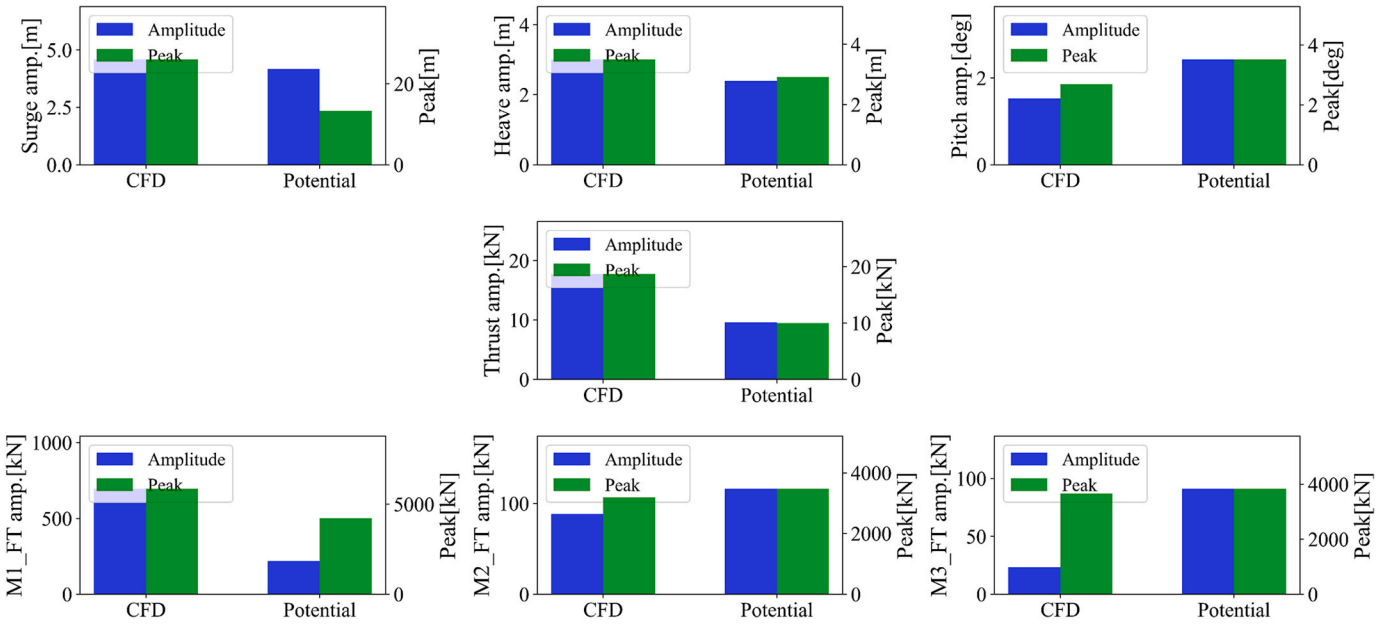

Fig. 14. Wave only considered extreme condition load response amplitude and peak value result code comparison.

4.3. Extreme environment condition code comparison result

Integrated load analysis in extreme environments was conducted to evaluate the degree of error that arises in the middle and high fidelity analysis tool for each load component, constituting the extreme environment. Analyses were performed under load conditions with waves only, with waves and wind, and with a combination of waves, wind, and current. These conditions reflect the extreme load situations caused by typhoons, with simulations and analyses carried out for turbines in a parking state. Therefore, the analysis of torque was excluded. To evaluate the error rate between analysis tools as well as the safety and stability of the system simultaneously, some load response results were normalized using reference values. For the mooring lines, nondimensionalization was based on the breaking load (MBL) of the mooring lines used in this study, which is 21,179 kN. Surge was nondimensionalized based on the point 63 m away in the horizontal direction from the incident load direction where the breaking load occurs. Heave and the point where the air-gap becomes zero, set at 16.5 m, were used as the basis for nondimensionalization, and pitch was nondimensionalized based on the capsizing point at 18.5°.

4.3.1. Wave only loading

Fig. 12 presents graphs comparing the system load response results of the two analysis tools under extreme environmental conditions considering only waves. Looking at the first three graphs (Surge, Heave, Pitch), in all instances, the CFD and Potential analysis results showed similar trends without significant discrepancies. Particularly in the results for Surge and Pitch, both analyses predicted almost identical periods and amplitudes. As shown in Fig. 14, the surge amplitude value was approximately within 4m, and the heave amplitude value was within

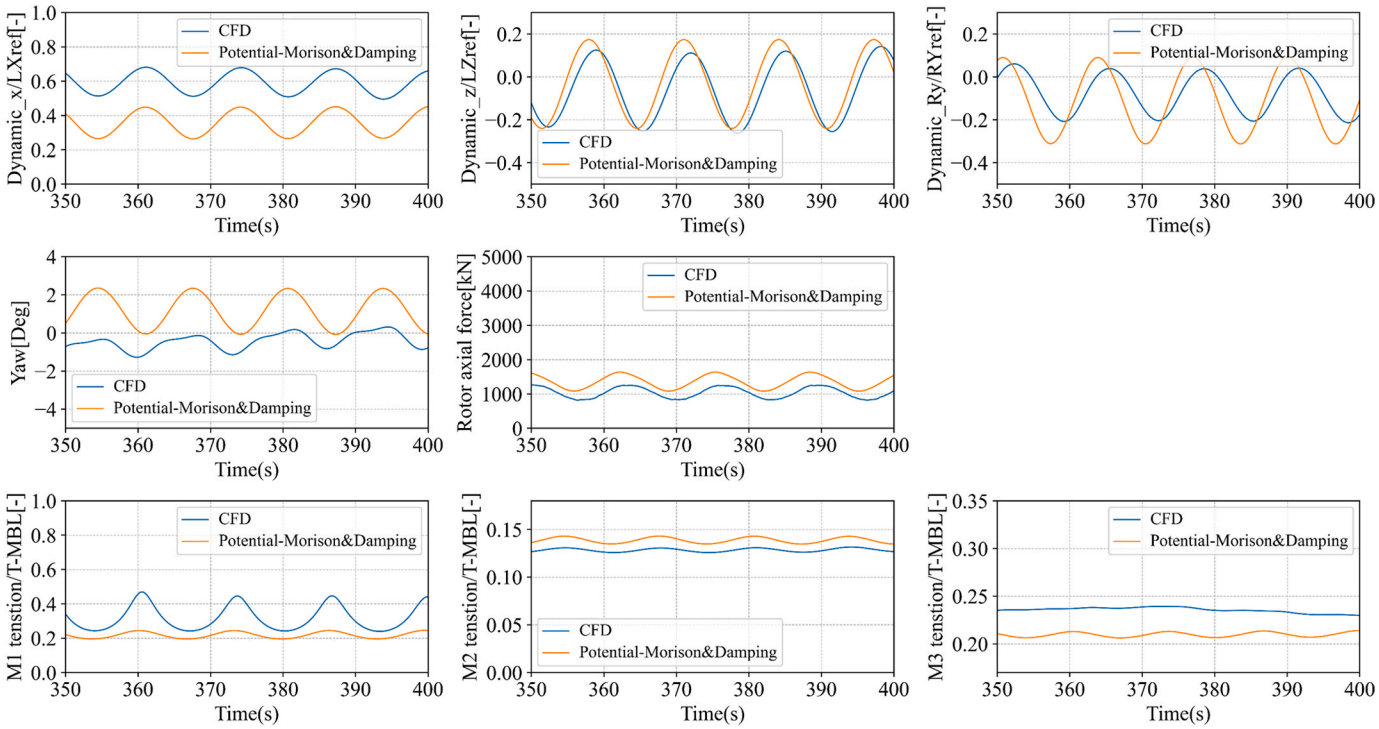

Fig. 15. Wave and wind considered extreme condition code comparison time series load response result.

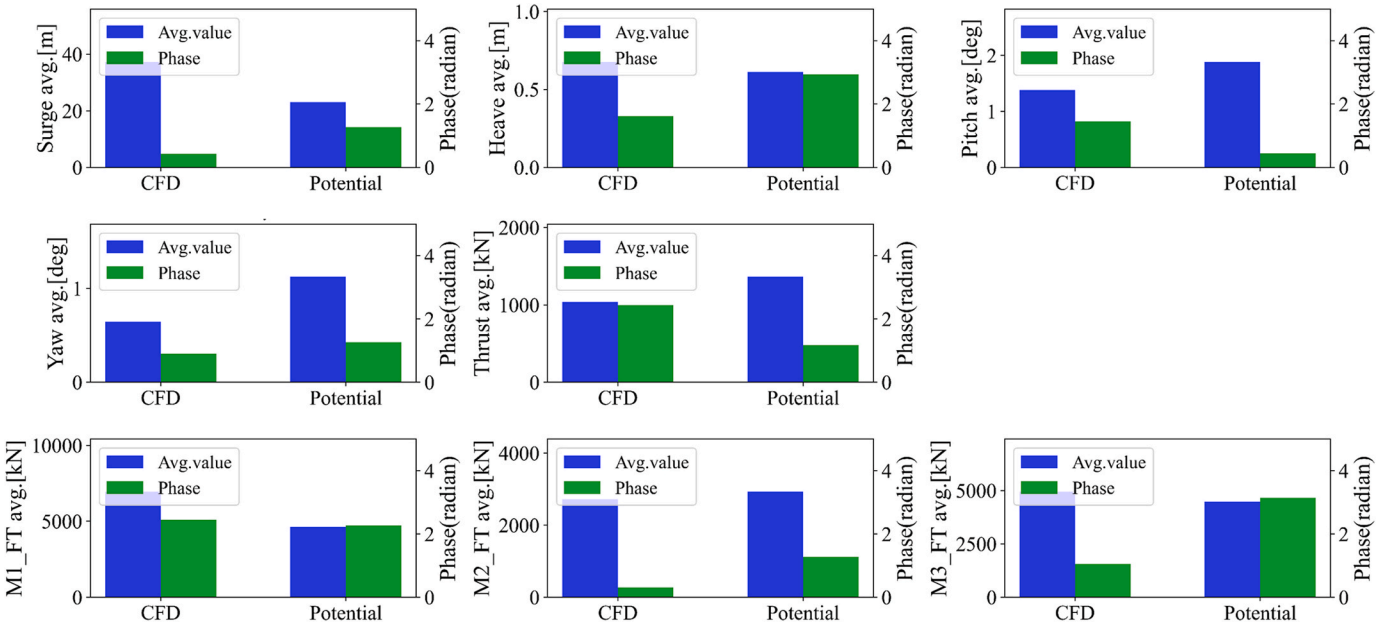

Fig. 16. Wave and wind considered extreme condition load response average and phase result code comparison.

3m. However, when comparing the average load response values as shown in Fig. 13, for surge, the CFD average was 21.49m while the Potential analysis tool average was 9.13m, indicating an under-response of approximately 12.4m by the Potential analysis tool. Conversely, in pitch motion, the Potential analysis tool showed an over-response of about 1.5 times, and there were also some discrepancies in phase, suggesting that some results did exhibit differences between the two analysis tools. For Yaw, the amplitude appeared nearly similar, but the results of the two analysis tools were opposite. Due to the lateral progressing load, a complex fluid flow occurred, leading the CFD to predict movement with two main frequencies, whereas the Potential tool, which doesn't account for complex fluid flows, predicted a monotonous movement with one main frequency. For the M1 tension value, a different pattern emerged between the two analysis tools, as the Potential tool responded in a lower average surge section compared to the CFD. For the same reasons, somewhat higher average responses were observed in M2 and M3 tensions using the Potential analysis tool.

4.3.2. *Wave and wind loading*

Fig. 15 displays the results of simulations considering both wave and wind. Similar to the previous results that only considered waves, the movements of surge, heave, and pitch displayed comparable patterns

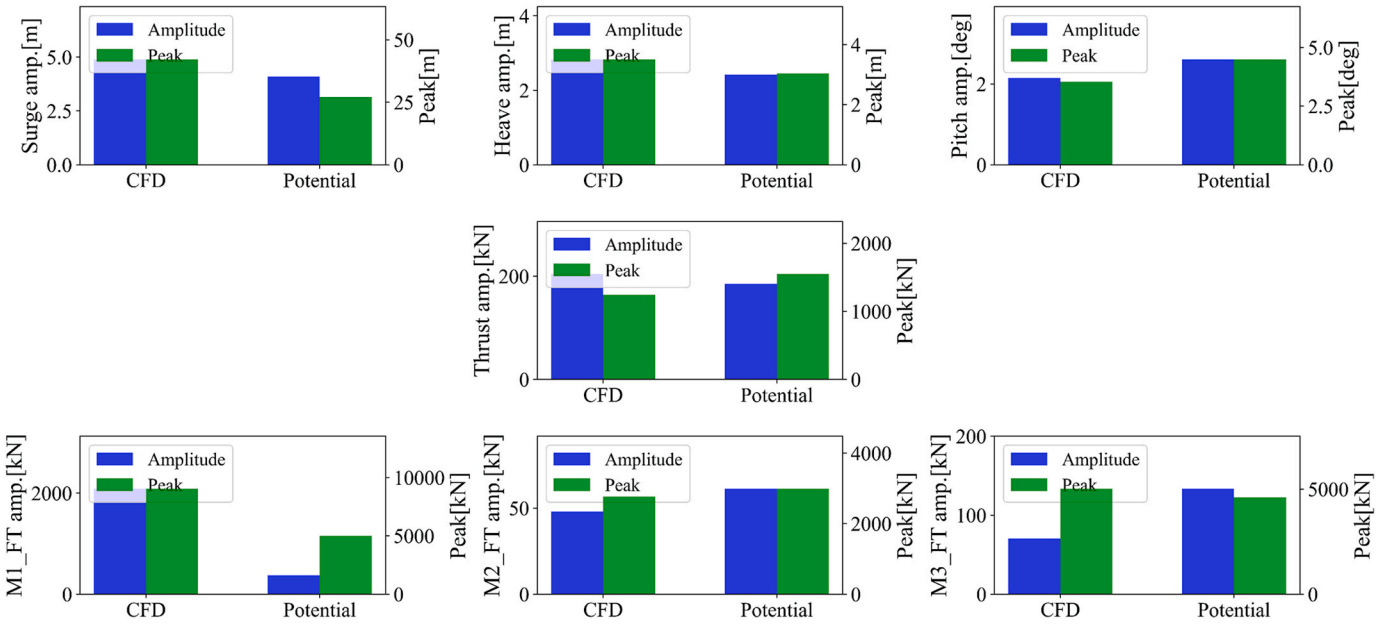

Fig. 17. Wave and wind considered extreme condition load response amplitude and peak value result code comparison.

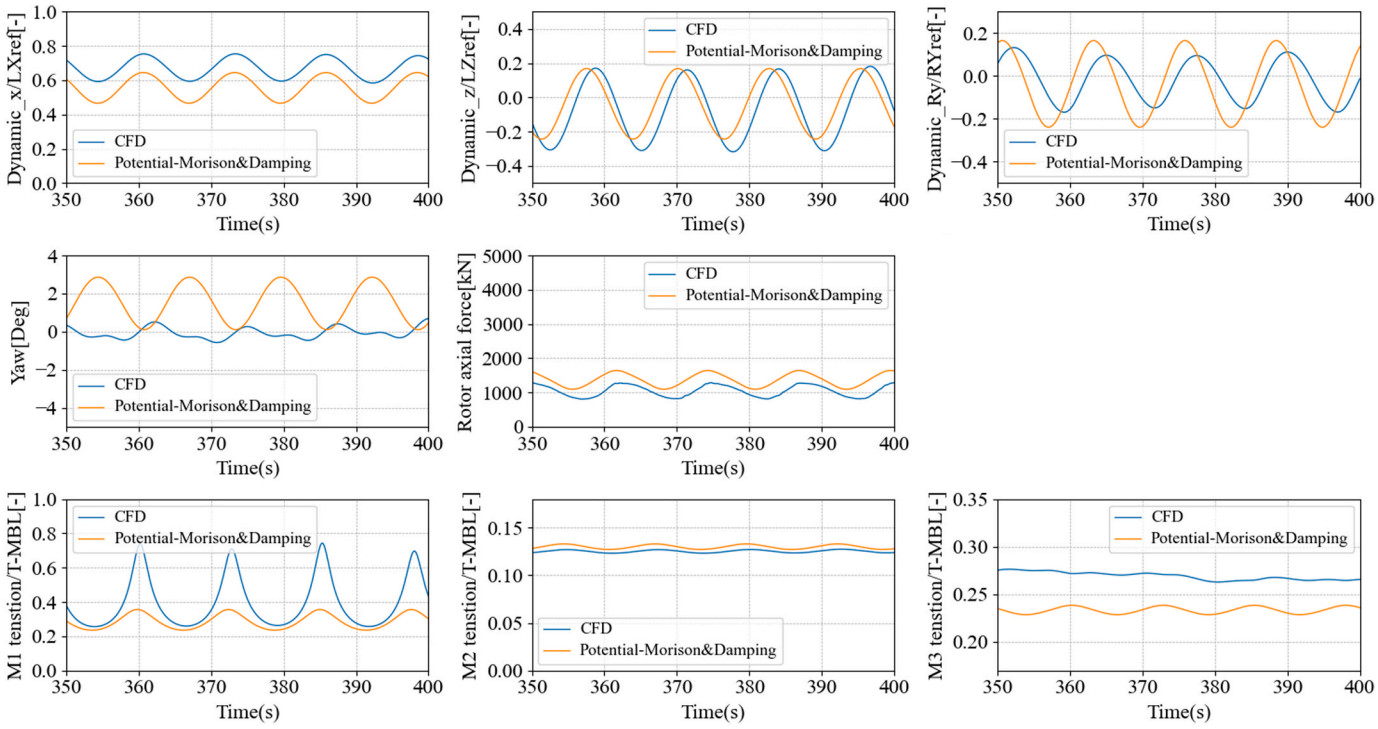

Fig. 18. All environment load considered extreme condition code comparison time series load response result.

between the two analysis tools without significant discrepancies. However, under the influence of strong wind speeds, as shown in Fig. 17, the amplitude of the surge response was approximately 4m in both analysis tools, very similar to the previous results. Furthermore, as observed in Fig. 16, the average surge response was 37.3m in CFD and 23.1m in the Potential analysis tool, showing an increase of about 14m in both methods compared to prior results. The movement in pitch, affected by the strong wind speed, led to a reduction in the differences between the two analysis tools. In contrast, the yaw motion showed a response direction almost identical to the previous one, with the amplitude being predicted to be slightly lower in the CFD. For the M1 tension response, due to the increased average surge response, there was a significant difference in the response characteristics acting on the mooring line.

4.3.3. *Wave, wind and current loading*

Fig. 18 represents the simulation results under an environment considering all load elements, namely; current, waves, and wind. Consistent with previous analysis results, the movements in surge, heave, and pitch displayed similar patterns between the two analysis tools. However, as observed from Fig. 19, due to the influence of the current, the surge movement in CFD increased to 42.2m, a 5m increase from the previous average load response. In contrast, the Potential

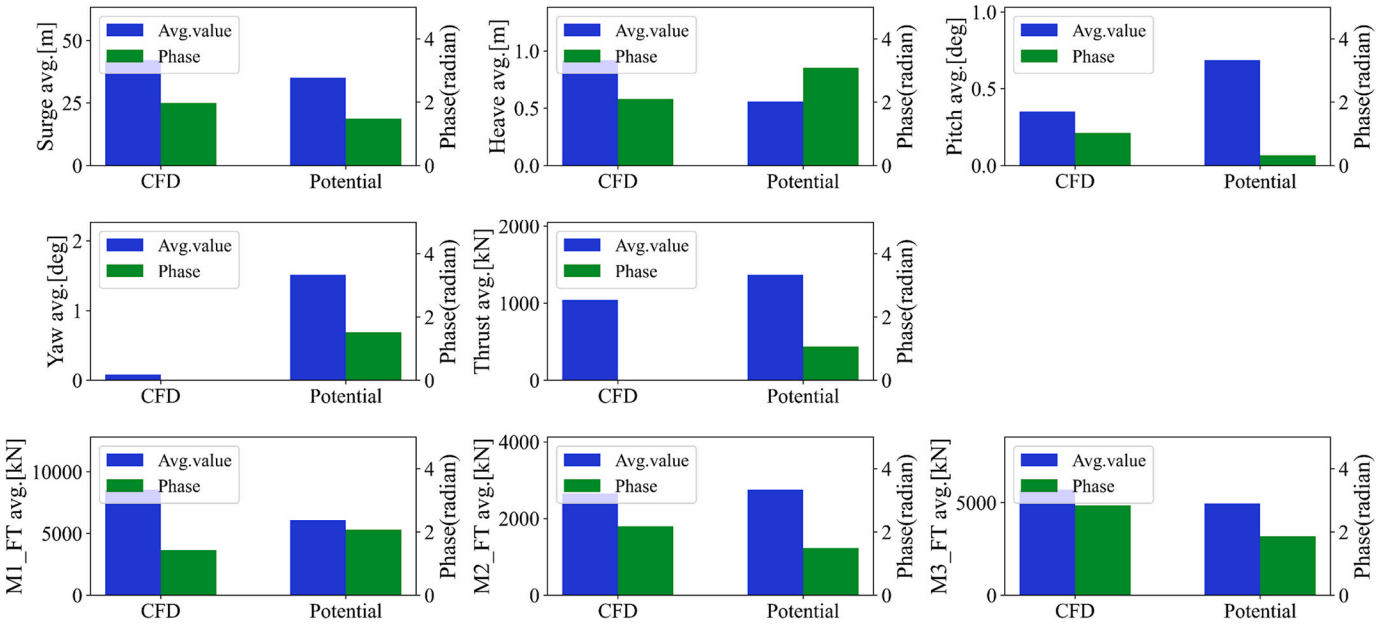

Fig. 19. All environment load considered extreme condition load response average and phase result code comparison.

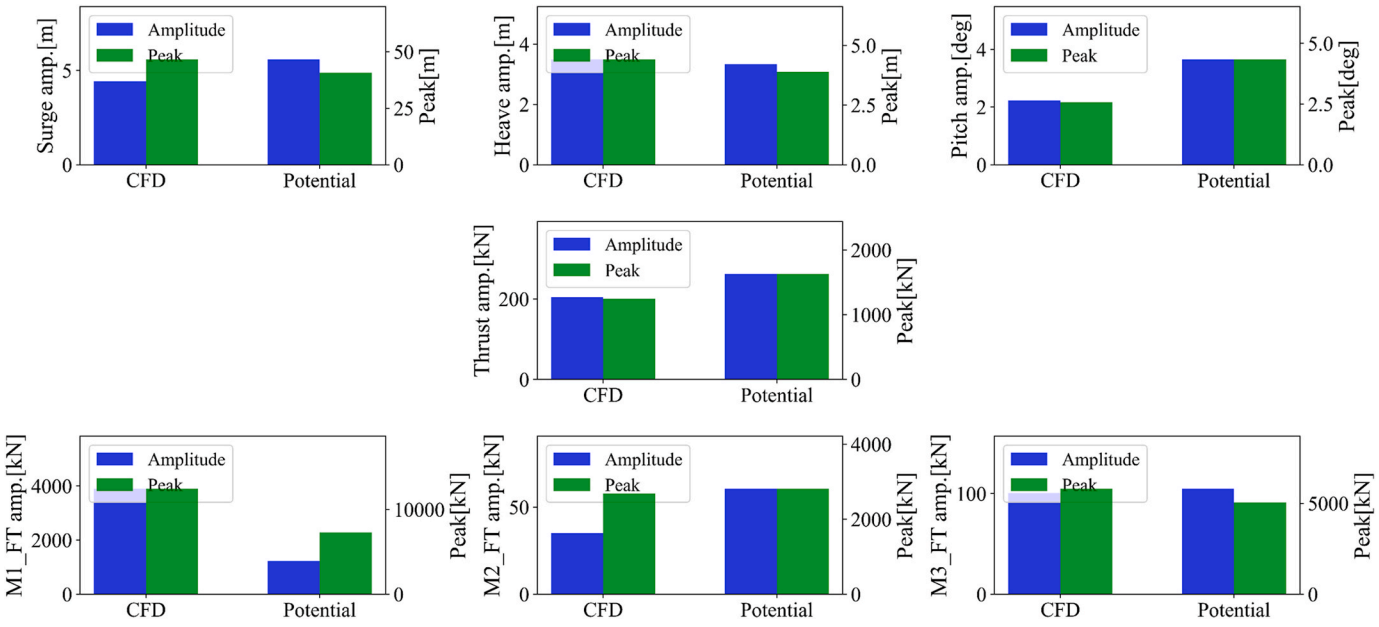

Fig. 20. All environment load considered extreme condition load response amplitude and peak value result code comparison.

analysis tool showed an increase to 35.1m, which is 12m higher than the scenario when current wasn't being considered. In this extreme environment with the current included, the Potential tool consistently underestimated the response in the Surge direction. However, due to the applied Morison drag coefficient in the composite method, the error was reduced to about 15%. Movements in heave and pitch were not significantly different between the two tools compared to the previous results. In yaw movement, irregularities occurred due to the vortex around the floater, but with the addition of the current, the CFD prediction reached almost 0 in average movement, with decreased amplitude. The thrust of the turbine showed no significant difference from the previous results. As observed in Fig. 19, the average surge response discrepancy was about 7m. Due to the elevated average surge response, the peak discrepancy in the load acting on the mooring line was considerably large, at approximately 5,127 kN.

Interestingly, examining the average response amplitude results in Fig. 20, the CFD showed almost no difference in load response amplitude due to a 0.77 m/s current, but with the potential method, the load response amplitude increased by about 1m in surge and about 1° in pitch. Additionally, as the pitch response amplitude increased, the thrust also increased by about 50 kN.

5. Conclusion

Previous research compared the CFD and Potential flow-based analysis tools under rated wind speed conditions without considering currents. The analysis primarily focused on 3 DoF, tension at the Fairlead, and results from the fairlead of the mooring line in the directions of surge, pitch, and the largest displacement, excluding heave.

The results showed a significant discrepancy in the surge response of

system displacement between the two tools, especially when damping and drag coefficients were not applied in the Potential flow-based tool. This study derived correction coefficients based on free-decay motion data obtained from CFD analysis to reflect appropriate viscous effects in middle fidelity analysis tools. Typically, free-decay results are used to derive damping coefficients. However, for marine floating structures where viscous effects cannot be ignored, applying only damping coefficients does not form an accurate drift response. Viscous effects can reflect individually for each load element using other correction methods, such as current load and wind load correction. However, these methods, which use load coefficients for fixed unit surface areas, are significantly limited in accuracy. Consequently, this study proposed a method of applying damping and drag coefficients to the Potential analysis tool complexly to adequately implement both damping motion and drift effects.

In the results of the extreme load condition simulation, when analyzing the outcomes from each load component between the analysis tools, a distinct discrepancy was observed in the average displacement of the floater in environments considering only waves. Although there was no significant difference in the response amplitude, the average response predicted by the potential analysis tool was lower compared to CFD. This led to differences in the loads acting on Mooring line 1(M1). In environments with strong wind, the wind-induced load amplified the discrepancy between the analysis tools. Furthermore, in extreme conditions with all load factors, including currents, the average surge offset increased. But, by using a correction method that applies the drag coefficient complexly with the damping coefficient to the Potential method tool, it became possible to simultaneously consider the drag effect caused by currents, thereby reducing the discrepancy between the analysis tools.

However, even after correcting the Floating Offshore Wind Turbine (FOWT) response in the potential method tool through CFD free-decay simulation, significant discrepancies occurred in all Design Load Case (DLC) simulations. This suggests limitations in correcting the floating structure response in the potential method tool using only free-decay results. Particularly, determining damping coefficient values through free-decay simulation while applying a general drag coefficient value, as done in this study, was a major factor causing significant discrepancies between the analysis tools. The default drag coefficient was not suitable for the floater used in this study, resulting in unimproved surge response discrepancies.

Yaw motion also showed significant discrepancies in average response and response characteristics in all DLC simulations even after correcting the FOWT response in the potential method tool through CFD free-decay simulation. Since the load acting on the mooring lines predominantly influences yaw response, it is expected that improving surge response prediction will significantly reduce yaw motion discrepancies.

In conclusion, this study confirmed that using only free-decay motion results as data for correcting the potential method tool is not appropriate. It was also found that correctly prioritizing the application of the drag coefficient over the damping coefficient is crucial for accurate prediction of the FOWT load response. Furthermore, for structures where the columns of the floater are connected by pontoons rather than braces, it was observed that wave drift force plays a significant role in the system load response. Based on these findings, future research will focus on more accurately reflecting wave drift force in the potential method tool for such floaters.

CRediT authorship contribution statement

Ho-Seong Yang: Writing – review & editing. **Ali Alkhabbaz:** Writing – review & editing, Visualization, Validation, Software. **Watchara Tongphong:** Visualization, Software. **Young-Ho Lee:** Writing – review & editing, Supervision, Funding acquisition.

Declaration of competing interest

The authors declare that they have no known competing financial interests or personal relationships that could have appeared to influence the work reported in this paper.

Data availability

Data will be made available on request.

Acknowledgements

This research was supported by Korea Institute of Energy Technology Evaluation and Planning (KETEP) grant funded by the Korean government (MOTIE) (20213000000030)—Development of disconnectable mooring system for A MW class floating offshore wind turbine.

Appendix A. Supplementary data

Supplementary data to this article can be found online at https://doi.org/10.1016/j.oceaneng.2024.117248.

References

Alkhabbaz, A., Yang, H.S., Weerakoon, A.H.S., Lee, Y.H., 2021. A novel linearization approach of chord and twist angle distribution for 10 KW horizontal Axis wind turbine. Renew. Energy 178, 1398–1420.
Alkhabbaz, A., Yang, H.S., Tongphong, W., Lee, Y.H., 2022. Impact of compact diffuser shroud on wind turbine aerodynamic performance: CFD and experimental investigations. Int. J. Mech. Sci. 216, 106978.
AZCONA, José, Bouchotrouch, Faisal, Vittori, Felipe, 2019. Low-frequency dynamics of a floating wind turbine in wave tank–scaled experiments with SiL hybrid method. Wind Energy 22 (10), 1402–1413.
Bak, Christian, Zahle, Frederik, Bitsche, Robert, Kim Anders Yde, Taeseong, Christian Henriksen, Lars, Natarajan, Anand, Hansen, Morten Hartvig, 2013. Description of the DTU 10 MW Reference Wind Turbine. Roskilde, DK: DTU Wind Energy. DTU Wind Energy Report-I-0092.
Bayati, I., Jonkman, J., Robertson, A., Platt, A., 2014. The effects of second-order hydrodynamics on a semisubmersible floating offshore wind turbine. J. Phys. Conf. 524, 012094.
Benitz, M.A., Schmidt, D.P., Lackner, M.A., Stewart, G.M., Jonkman, J., Robertson, A., 2014. Comparison of hydrodynamic load predictions between reduced order engineering models and computational fluid dynamics for the OC4-DeepCwind semi-submersible. In: Proceedings of the ASME 2014 33rd International Conference on Ocean, Offshore and Arctic Engineering, ume 9B. Ocean Renewable Energy, San Francisco, California, USA. June 8–13, 2014. V09BT09A006. ASME.[.
Benitz, M.A., Schmidt, D.P., Lackner, M.A., Stewart, G.M., Jonkman, J., Robertson, A., 2015. Validation of hydrodynamic load models using CFD for the OC4-DeepCwind semisubmersible. In: Proceedings of the ASME 2015 34th International Conference on Ocean, Offshore and Arctic Engineering, ume 9. Ocean Renewable Energy, St. John's, Newfoundland, Canada. May 31–June 5.
Böhm, M., Robertson, A., Hübler, C., Rolfes, R., Schaumann, P., 2020. Optimization-based calibration of hydrodynamic drag coefficients for a semisubmersible platform using experimental data of an irregular sea state. J. Phys. Conf. Ser. 1669, 012023.
Cheng, P., Huang, Y., Wan, D., 2019. A numerical model for fully coupled aero-hydrodynamic analysis of floating offshore wind turbine. Ocean Eng. 173, 183–196.
Delany, K., Sorensen, E., 1953. Low-speed Drag of Cylinders of Various Shapes. Nat. Adv. Comm. Aero., Washington. Technical Note 3038.
DNV, 2021. ST-0119, Floating Wind Turbine Structures.
Edirisinghe, D.S., Yang, H.S., Gunawardane, S.D.G.S.P., Alkhabbaz, A., Tongphong, W., Yoon, M., Lee, Y.H., 2023. Numerical and experimental investigation on water vortex power plant to recover the energy from industrial wastewater. Renew. Energy 204, 617–634.
Ghalandari, M., Mukhtar, A., Shah, A., Yasir, H., Alkhabbaz, A., Alviz-Meza, A., Escrocia, Y., Le, B.N., 2023. Thermal conductivity improvement in a green building with Nano insulations using machine learning methods. Energy Rep. 9, 4781–4788.
Hamdoon, O.M., 2020. Improving the performance of a flat plate solar collector using nanofluid as working fluid. Al-Rafidain Engineering Journal (AREJ) 25 (2), 37–45.
Hussein, H.J., Dawood, A.S., 2021. Conjugate heat transfer of nanofluid flow inside a micro-wavy channel. Al-Rafidain Engineering Journal (AREJ) 26 (2), 201–210.
IEC, 2019. TS-61400-3-2, Wind Energy Generation Systems – Part 3-2: Design Requirements for Floating Offshore Wind Turbines.
Jonkman, J.M., 2013. The new modularization framework for the FAST Wind Turbine CAE Tool. In: Proceedings of the 51st AIAA Aerospace Sciences Meeting Including the New Horizons Forum and Aerospace Exposition. Grapevine, TX, USA, 7–10 January 2013.
LIFES50+ project, 2015, D7.2 Design Basis.
Lindsey, W.F., 1923. Drag of Cylinders of Simple Shapes. Report No. 619.

Liu, Y., Xiao, Q., Incecik, A., Peyrard, C., Wan, D., 2017. Establishing a fully coupled CFD analysis tool for floating offshore wind turbines. Renew. Energy 112, 280–301.
Liu, Y., Xiao, Q., Incecik, A., Peyrard, C., 2018. Aeroelastic Analysis of a Floating Offshore Wind Turbine in Platform-Induced Surge Motion Using a Fully Coupled CFD-MBD Method. Wind Energy.
Pegalajar-Jurado, A., Bredmose, H., 2019. Reproduction of slow-drift motions of a floating wind turbine using second-order hydrodynamics and Operational Modal Analysis. Mar. Struct. 66, 178–196.
Robertson, A., Jonkman, J., Masciola, M., Song, H., Goupee, A., Coulling, A., Luan, C., 2014. Definition of the Semisubmersible Floating System for Phase II of OC4. National Renewable Energy Lab (NREL), Golden, CO, USA.
Robertson, A.N., Wendt, F., Jonkman, J.M., Popko, W., Dagher, H., Gueydon, S., Qvist, J., Vittori, F., Azcona, J., Uzunoglu, E., Soares, C.G., Harries, R., Yde, A., Galinos, C., Hermans, K., de Vaal, J.B., Bozonnet, P., Bouy, L., Bayati, I., Bergua, R., Galvan, J., Mendikoa, I., Sanchez, C.B., Shin, H., Oh, S., Molins, C., Debruyne, Y., 2017. OC5 project phase II: validation of global loads of the DeepCwind floating semisubmersible wind turbine. Energy procedia; 14th deep sea offshore wind R&D conference. EERA DeepWind 137, 38–57, 2017.
Robertson, A.N., Gueydon, S., Bachynski, E., Wang, L., Jonkman, J., Alarcón, D., Amet, E., Beardsell, A., Bonnet, P., Boudet, B., Brun, C., Chen, Z., Féron, M., Forbush, D., Galinos, C., Galvan, J., Gilbert, P., Gómez, J., Harnois, V., Haudin, F., Hu, Z., Dreff, J.L., Leimeister, M., Lemmer, F., Li, H., Mckinnon, G., Mendikoa, I., Moghtadaei, A., Netzband, S., Oh, S., Pegalajar-Jurado, A., Nguyen, M.Q., Ruehl, K., Schünemann, P., Shi, W., Shin, H., Si, Y., Surmont, F., Trubat, P., Qwist, J., Wohlfahrt-Laymann, S., 2020. OC6 Phase I: investigating the underprediction of low-frequency hydrodynamic loads and responses of a floating wind turbine. J. Phys. Conf. 1618, 032033.
Sarpkaya, T., Isaacson, M., 1981. Mechanics of Wave Forces on Offshore Structures. Van Nostrand Reinhold, New York, NY, pp. 651–652.
Simos, A.N., Sparano, J.V., Aranha, J.A.P., Matos, V.L.F., 2008. 2nd Order Hydrodynamic Effects on Resonant Heave, Pitch and Roll Motions of a Large-Volume Semi-submersible Platform, pp. 229–237.
Simos, A.N., Ruggeri, F., Watai, R.A., Souto-Iglesias, A., Lopez-Pavon, C., 2018. Slow-drift of a floating wind turbine: an assessment of frequency-domain methods based on model tests. Renew. Energy 116, 133–154.
Srinivas, A., Robertson, B., Gadasi, J.B., Simpson, B.G., Lomónaco, P., Ilzarbe, J.M.B., 2023. Impact of limited degree of freedom drag coefficients on a floating offshore wind turbine simulation. J. Mar. Sci. Eng. 11, 139.
Venugopal, V., Varyani, K.S., Westlake, P.C., 2009. Drag and inertia coefficients for horizontally submerged rectangular cylinders in waves and currents. Proc. IME M J. Eng. Marit. Environ. 223, 121–136.
Wang, L., Robertson, A., Jonkman, J., Yu, Y., Koop, A., Borràs Nadal, A., Li, H., Bachynski-Polić, E., Pinguet, R., Shi, W., Zeng, X., Zhou, Y., Xiao, Q., Kumar, R., Sarlak, H., Ransley, E., Brown, S., Hann, M., Netzband, S., Wermbter, M., Méndez López, B., 2021a. OC6 Phase Ib: validation of the CFD predictions of difference-frequency wave excitation on a FOWT semisubmersible. Ocean Eng. 241, 110026.
Wang, L., Robertson, A., Jonkman, J., Yu, Y.-H., 2021b. Uncertainty assessment of CFD investigation of the nonlinear difference-frequency wave loads on a semisubmersible FOWT platform. Sustainability 13, 64. https://doi.org/10.3390/su13010064.
Yang, H.S., Alkhabbaz, A., Edirisinghe, D.S., Tongphong, W., Lee, Y.H., 2022. FOWT stability study according to number of columns considering amount of materials used. Energies 15, 1653.
Yang, H.S., Tongphong, W., Alkhabbaz, A., Lee, Y.H., 2023. Different fidelity hydrodynamic-aerodynamic coupled simulation code on the 10 MW semi-submersible type floating offshore wind turbine. Ocean Eng. 281.
Yao, Tian-Cheng, et al., 2020. CFD-based analysis of a 6MW spar-type floating wind turbine with focus on nonlinear wave loads. In: ISOPE International Ocean and Polar Engineering Conference. ISOPE.
Zhou, Y., Xiao, Q., Liu, Y., Incecik, A., Peyrard, C., Li, S., Pan, G., 2019. Numerical modelling of dynamic responses of a floating offshore wind turbine subject to focused waves. Energies 12, 3482. https://doi.org/10.3390/en12183482.